iScience

CellPress
OPEN ACCESS

Article

A wireless optoelectronic skin patch for light delivery and thermal monitoring

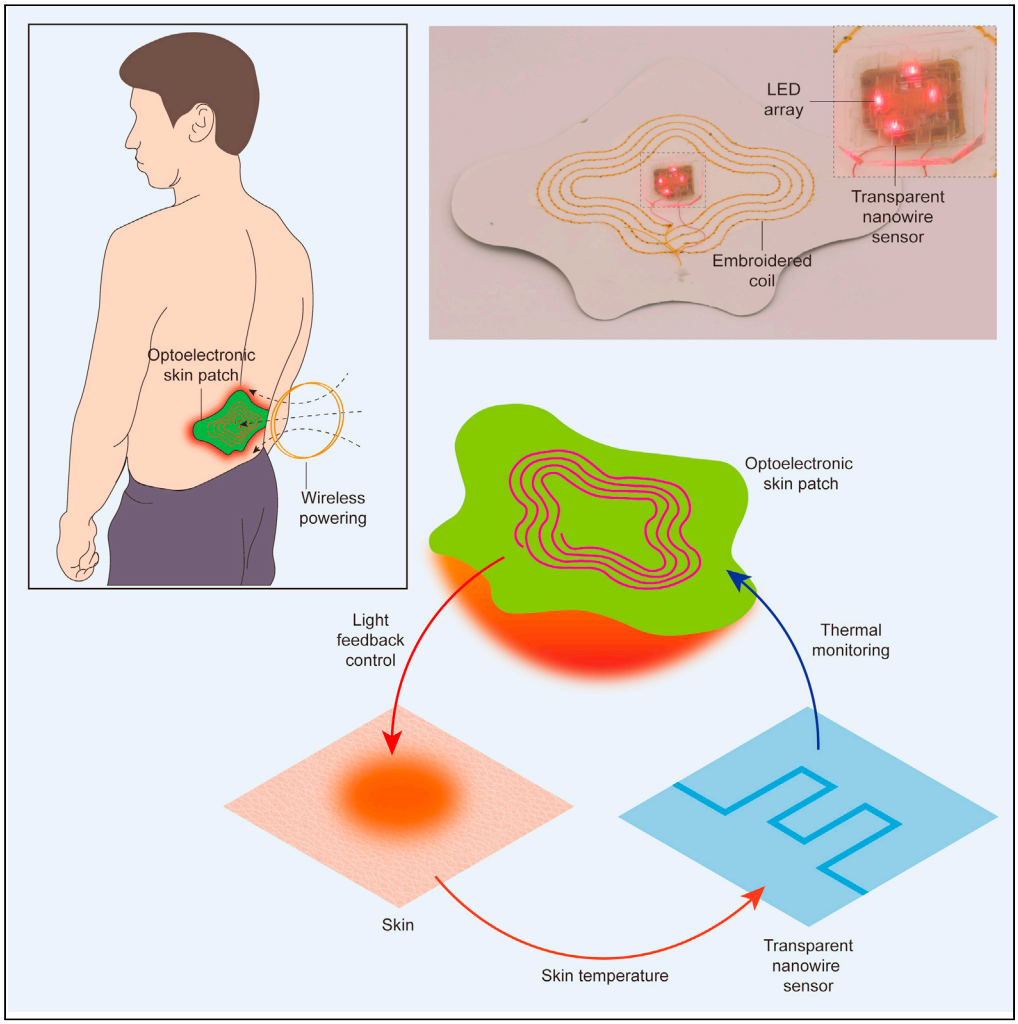

Han-Joon Kim, Yunxia Jin, Sippanat Achavananthadith, Rongzhou Lin, John S. Ho

johnho@nus.edu.sg

Highlights

A wireless optoelectronic patch measures photothermal effects on the skin

A transparent nanowire sensor enables co-located light delivery and thermal monitoring

Experiments demonstrate closed-loop thermal regulation and blood flow monitoring

Kim et al., iScience *24*, 103284
November 19, 2021
https://doi.org/10.1016/j.isci.2021.103284

iScience

CellPress
OPEN ACCESS

Article

A wireless optoelectronic skin patch for light delivery and thermal monitoring

Han-Joon Kim,[1] Yunxia Jin,[2] Sippanat Achavananthadith,[1] Rongzhou Lin,[2] and John S. Ho[1,2,3,4,*]

SUMMARY

Wearable optoelectronic devices can interface with the skin for applications in continuous health monitoring and light-based therapy. Measurement of the thermal effect of light on skin is often critical to track physiological parameters and control light delivery. However, accurate measurement of light-induced thermal effects is challenging because conventional sensors cannot be placed on the skin without obstructing light delivery. Here, we report a wearable optoelectronic patch integrated with a transparent nanowire sensor that provides light delivery and thermal monitoring at the same location. We achieve fabrication of a transparent silver nanowire network with >92% optical transmission that provides thermoresistive sensing of skin temperature. By integrating the sensor in a wireless optoelectronic patch, we demonstrate closed-loop regulation of light delivery as well as thermal characterization of blood flow. This light delivery and thermal monitoring approach may open opportunities for wearable devices in light-based diagnostics and therapies.

INTRODUCTION

Skin-mounted optoelectronic devices offer important capabilities for remote health monitoring and delivery of light-based treatments. Owing to their intimate integration with skin, such devices can precisely measure tissue optical properties and continuously monitor a wide range of physiological parameters, such as heart rate, oxygen saturation, and hemodynamic activity (Kim et al. 2017b, Kim et al., 2016; Webb et al. 2015a; Yu et al., 2020; Kang et al., 2021). They can also provide light delivery for therapeutic applications—through the activation of chemical reactions (photodynamic) (Bansal et al., 2018; Fritsch et al., 1998; Dolmans et al., 2003), generation of heat (photothermal), or modulation of biological processes (Shao et al., 2016; Ren et al., 2015; Juarranz et al., 2008) (photobiomodulation) (Chung et al., 2012; Hamblin et al., 2019)—with greater convenience and versatility than standard light sources currently used in the clinic in the form of wired handheld or fixture-mounted lamps (Terman and Terman, 2005). When integrated with wireless technologies such as near-field communication (NFC), such devices can further achieve digital data transmission and be wirelessly recharged, which can enable diagnosis and treatment to take place in a variety of settings outside of the clinic (Watthanawisuth et al. 2010; Garbarino et al. 2014; Yu et al., 2020; Safaie et al., 2013; Kang et al., 2021; Jeong et al., 2019).

Integrating thermal monitoring capabilities with wearable optoelectronic devices is critical for many clinical applications. For example, measuring the thermal effect of light on skin can provide important information about dermatological health, such as skin hydration, structure, and thermoregulation (Gao et al., 2014; Kim et al., 2016; Jeong et al., 2019). By measuring the heating profile induced by light at multiple points on the skin, hemodynamic activity such as blood flow and perfusion can also be revealed (Webb et al. 2015a, 2015b; Kim et al., 2016; Devor et al., 2012). These diagnostic applications generally involve low optical power densities (<10 $mWcm^{-2}$) and minimal thermal effect (<1°C) (Wyser et al., 2017), whereas therapeutic applications generally involve higher optical power densities (ranging from 20 $mWcm^{-2}$ to 1.9 Wcm^{-2}, Table 1) that may involve risk of thermal damage to tissues. In these applications, thermal monitoring is essential to regulate the optical output and maintain safe levels of exposure (IEEE 2006; Bashkatov et al., 2005). However, accurate measurement of light-induced thermal effects is currently hindered by the lack of a suitable sensor. Infrared sensors, for example, are widely used in the clinic and are capable of non-contact thermal measurement, but require stable optical configurations that are difficult to achieve with a wearable device (Webb et al. 2015b; Beigzadeh et al., 2020; Wilson and Patterson 2008). Alternatively, contact-based thermal sensors, such as thermocouples and thermoresistors, can be fabricated in

[1]Department of Electrical and Computer Engineering, National University of Singapore, Singapore 117583, Singapore

[2]Institute for Health Innovation and Technology, National University of Singapore, Singapore 117599, Singapore

[3]The N.1 Institute for Health, National University of Singapore, Singapore 117456, Singapore

[4]Lead contact

*Correspondence: johnho@nus.edu.sg

https://doi.org/10.1016/j.isci.2021.103284

Table 1. Requirements for light-based diagnostic and therapeutic applications

Techniques	Light intensity ($mWcm^{-2}$)	Wavelength (nm)	Skin penetration depth (mm) (Bashkatov et al., 2005)	Ref.
Pulse oximetry	≤ 1	600–1,000	1.5–2.8	Khan et al., 2018; Jinno et al., 2021; Kim et al., 2016
Functional near-infrared spectroscopy	≤ 10	700–1,000	2–2.8	Wyser et al., 2017
UV light therapy	20–80	290–320	< 0.1	Zhang et al., 2021
Photobiomodulation	≤ 100	400–1,200	~0.3–3.5	Zein et al., 2018
Photodynamic	50–150	400–700	~0.3–2	Bäumler (2001)
Photothermal	900–1900	700–1,000	2–2.8	Cortezon-Tamarit et al. (2017); Eskiizmir et al. (2017)

Applications generally require >1 cm^2 illumination area.

flexible formats and placed directly on the skin for monitoring auxiliary and ambient temperature (Jeong et al., 2019; Kang et al., 2021; Kim et al., 2016; Wang et al., 2020; Yun et al., 2019). However, existing forms of these sensors are optically opaque and obstruct light delivery, which introduces uncertainty due to the need for calibration models and limits their utility for monitoring light-induced thermal effects. Highly miniaturized thermal sensors have also been developed, but either provide monitoring at only a single point or require an array of sensors with complex interconnects.

Recent advances in transparent electronics have yielded a wide range of strategies to fabricate flexible and transparent sensors (Langley et al., 2013). These strategies are based on nanomaterials, such as metallic nanowires, carbon nanotubes, and reduced graphene oxide (rGO), to achieve flexible transparent films that overcome the brittleness of conventional transparent conductive oxides (Wu et al., 2020). In particular, silver nanowires (AgNWs) have been used to realize films with high optical transparency, electrical conductivity, and mechanical flexibility. Such films have been explored for solar cells (Thomas et al., 2018; Zhang et al. 2019a), touch panels (Yang et al., 2019), organic light-emitting diodes (LEDs) (Kim et al. 2017a), and sensors (Shin et al., 2020; Choi et al., 2020), but their integration to wearable optoelectronic devices has not been previously demonstrated.

Here, we report a wearable optoelectronic patch that provides wireless light delivery with thermal monitoring of skin. In particular, we fabricated an AgNW network that exhibits >92% optical transmission across the visible spectrum and senses temperature through the thermoresistive effect. We integrated this transparent sensor into a wirelessly powered optoelectronic patch to realize light delivery and thermal monitoring at the same location on the skin. With this device, we demonstrate closed-loop light delivery in which feedback from the thermal sensor is used to regulate the optical output and maintain a target skin temperature with a faster response time than a non-transparent thermocouple. We also demonstrate the capability of the optoelectronic patch to monitor blood flow by measurement of the heating profile of skin resulting from optical illumination.

RESULTS

System concept and design

Figure 1A shows a schematic of the wearable optoelectronic patch for light delivery and thermal monitoring on skin. The device comprises an LED array, a transparent thermal sensor, a wireless energy harvesting circuit, and a planar inductor embroidered on a fabric skin patch. Wireless power transfer from a nearby transmitter, which can be a smartphone or a coil placed on the surface of a chair or bed (Blouin et al., 1996), enables the device to operate in a battery-free manner and achieve a thin, lightweight form factor suitable for mounting onto the skin. For continuous use during daily life, a small battery may be incorporated into the patch such that proximity with the wireless transmitter is required only during recharging (Lee et al. 2020b). The LEDs were selected to have a peak emission wavelength at 660 nm, which is relevant to a wide range of applications including pulse oximetry, photodynamic therapy, and photobiomodulation (Table 1). The transparent thermal sensor is mounted directly on the LED array where it can interface

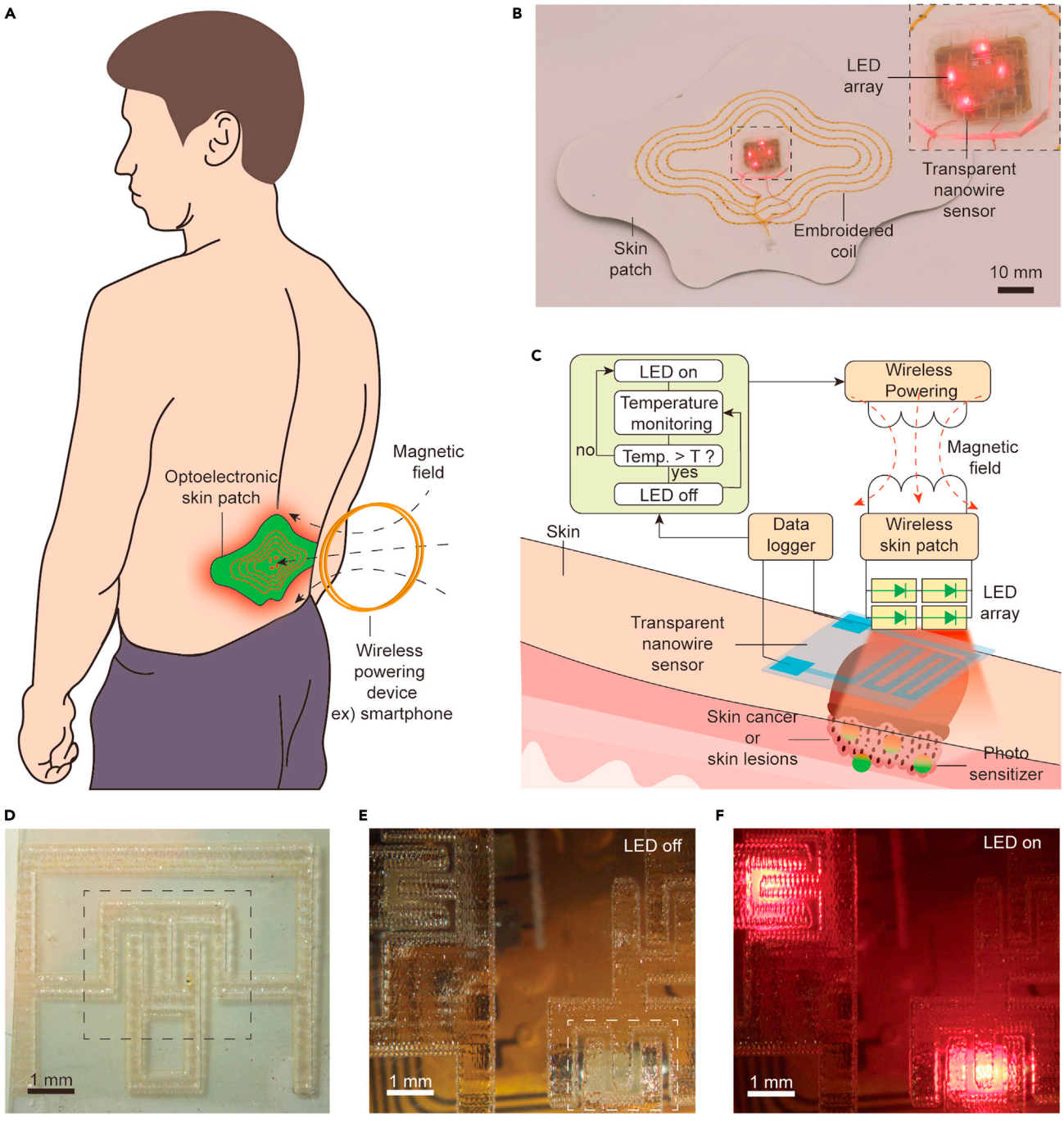

Figure 1. Wireless optoelectronic patch and integrated transparent sensor

(A) Illustration of the skin-mounted optoelectronic patch and wireless power transfer system.

(B) Image of the wirelessly powered optoelectronic patch. Inset shows the LED array with integrated transparent temperature sensor.

(C) Schematic of the wireless system. The optoelectronic patch is wirelessly powered by external controller, which uses sensor data to regulate light delivery.

(D) Image of the transparent sensor on a uniform background.

(E) Image of the transparent temperature sensor array placed on an inactive LED array. The white dotted line outlines the sensor above an LED.

(F) Image of the transparent sensor array with activated LED array.

with the skin to monitor temperature at the location of light delivery (Figure 1B). Upon activation, the LED array emits light through a transparent temperature sensor, which provides digitized temperature data through a data logger. These data can be wirelessly communicated via NFC or Bluetooth to the wireless power transmitter, enabling the LED output to be regulated by a control algorithm (Figure 1C). We implemented a simple, threshold-based binary control algorithm to maintain the time-averaged temperature at the target level, although the system is compatible with a broad range of control techniques. Figures 1D–1F show that the thermal sensor allows high transmission of light from the LED array.

Fabrication of the transparent thermal sensor

The transparent sensor is fabricated by patterning AgNW film with laser-induced ablation (Figure 2A). This process provides one-step, non-contact, and computer-controlled patterning with microscale resolution without the cost and complexity of photolithography. By controlling the laser energy and scanning speed, AgNW film can be patterned to conductive meandered lines with width as small as 150 μm (Figure 2B). Figure 2C shows a scanning electron microscopic (SEM) image of the AgNW networks after laser ablation. The surface morphology shows highly consistent, randomly distributed AgNWs that are free of damage from laser energy. The image also shows a layer of rGO coated on the AgNW film, which improves the conductivity of the film by increasing contact between the nanowire junctions.

Figure 2D shows a transparent sensor array fabricated using this process. We evaluated the transparency of the array using optical transmission measurements (Figure 2E). The transmittance is 92% at 660 nm, which is among the highest achieved in a conductive film to date (Table S1 (Jin et al., 2015, Jin et al., 2018; Zhang et al. 2019b; Tang et al., 2019; Yang et al., 2020; Bi et al., 2019), and is highly uniform across the visible spectrum. Optical images of the array placed over a colored blue mark (Figure 2F) and background text (Figure 2G) highlight the visual transparency of the fabricated sensor. We characterized the sensitivity of the thermal sensor in terms of the thermal coefficient of resistance α, defined as (Cui et al., 2019),

$$\alpha = \frac{1}{R(T_0)} \frac{R(T) - R(T_0)}{T - T_0} \quad \text{(Equation 1)}$$

where $R(T_0)$ is the resistance at room temperature T_0=25°C and $R(T)$ is the resistance at the operating temperature T. Bulk Ag has an α of $3.8\times10^{-3}{}^{\circ}C^{-1}$ at 20°C, which is close to that of other widely used thermoresistive materials, such as Pt. To realize transparent sensor, however, the areal density must be reduced, which generally results in lower α compared with the bulk material. Figure 2H shows the resistance of 6-turn sensor pattern (dimensions 1.5 mm × 2 mm) compared with that of the unpatterned film as a function of temperature. When the temperature is increased from 21°C to 100°C, R increases linearly from 809 to 942 Ω for the sensor pattern and 212 to 246 Ω for the unpatterned film. This indicates that α is similar for the patterned sensor ($2.05\times10^{-3}{}^{\circ}C^{-1}$) and the unpatterned film (α=$2.00\times10^{-3}{}^{\circ}C^{-1}$), suggesting that the patterning process preserves the nanostructure of the film (Figure 2I). As expected, α for the transparent sensor is lower than that of bulk silver owing to the reduced density (about 14 nanowires μm^{-2}), but the small patterned sensor works as well as the big unpatterned film. We further tested the response of the sensor in free space when driving current through the LED array (Figure 2J). The sensor exhibits a relative change in resistance of 0.5×10^{-3} per 1 mW of input power to the LED, which can be primarily attributed to the diffusion of electrically generated heat from the LED through the polydimethylsiloxane (PDMS) encapsulation layer.

Design of the optoelectronic wireless power transfer system

We designed a wireless power transfer system to enable the optoelectronic path to operate in an untethered manner. Figure 3A shows the design parameters of the system comprising two inductively coupled coils operating at 13.56 MHz, which is compatible with NFC technology in smartphones. The transmitter coil is connected with a signal generator via an L-type matching network, whereas the receiver circuit consists of a half-wave voltage doubler and an LED array (Figure 3B). The voltage doubler and impedance matching circuit between the load and coil are implemented using two Schottky diodes (BAT2402LSE6327XTSA1CT-ND, Infineon Technologies) and surface-mount capacitors. The load consists of an array of 660-nm LEDs (SML-LX0603SRW-TR, Lumex) connected in parallel with series resistors. We optimized the geometry of the coil and the impedance matching network for maximum power transfer efficiency under size and material constraints. The selected design parameters, summarized in Table 2, yield an S_{11} spectrum (measured from the input of the LED array) that indicates optimal operation at the desired operating frequency (Figure 3C). To provide conformal adhesion to the skin, the designed inductor

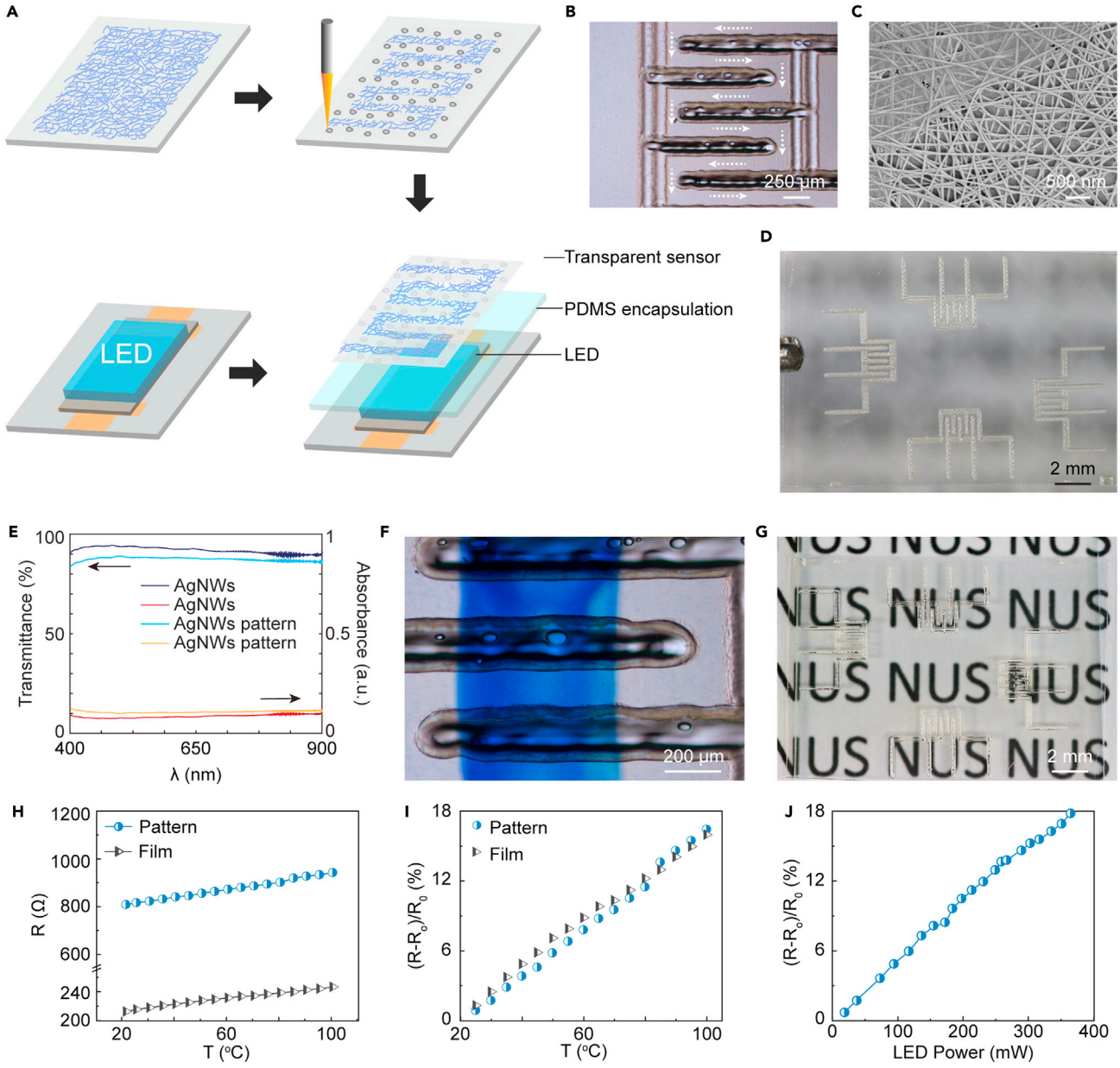

Figure 2. Fabrication and characterization of the transparent nanowire sensor

(A) Schematic of the fabrication process. AgNW film is selectively removed by laser-induced ablation to yield the desired pattern.

(B) Optical microscopy image of the sensor. White arrows show the nanowire path.

(C) SEM image of an intact region of the AgNW film after patterning.

(D) Image of the fabricated sensor array.

(E) Transmittance and absorbance spectra of the AgNW film before and after ablation following sensor design pattern.

(F) Optical microscopy image of the sensor. The bottom side of the sensor is marked in blue to highlight the transparency.

(G) Image of the sensor array on a lettered background.

(H) Resistance of the patterned sensor and AgNW film as a function of temperature.

(I) Relative change in resistance as a function of temperature.

(J) Relative change in resistance of the integrated sensor as a function of electrical power input to the LED array in free space.

is fabricated by embroidering thin copper thread (t_{rx}=0.16 mm) onto a medical skin patch composed of nonwoven fabric and an adhesive layer using a digital embroidery machine (NV180, Brother). The width of the patch is 100 mm and the height is 80 mm, which enables the inductive coil to be large enough to

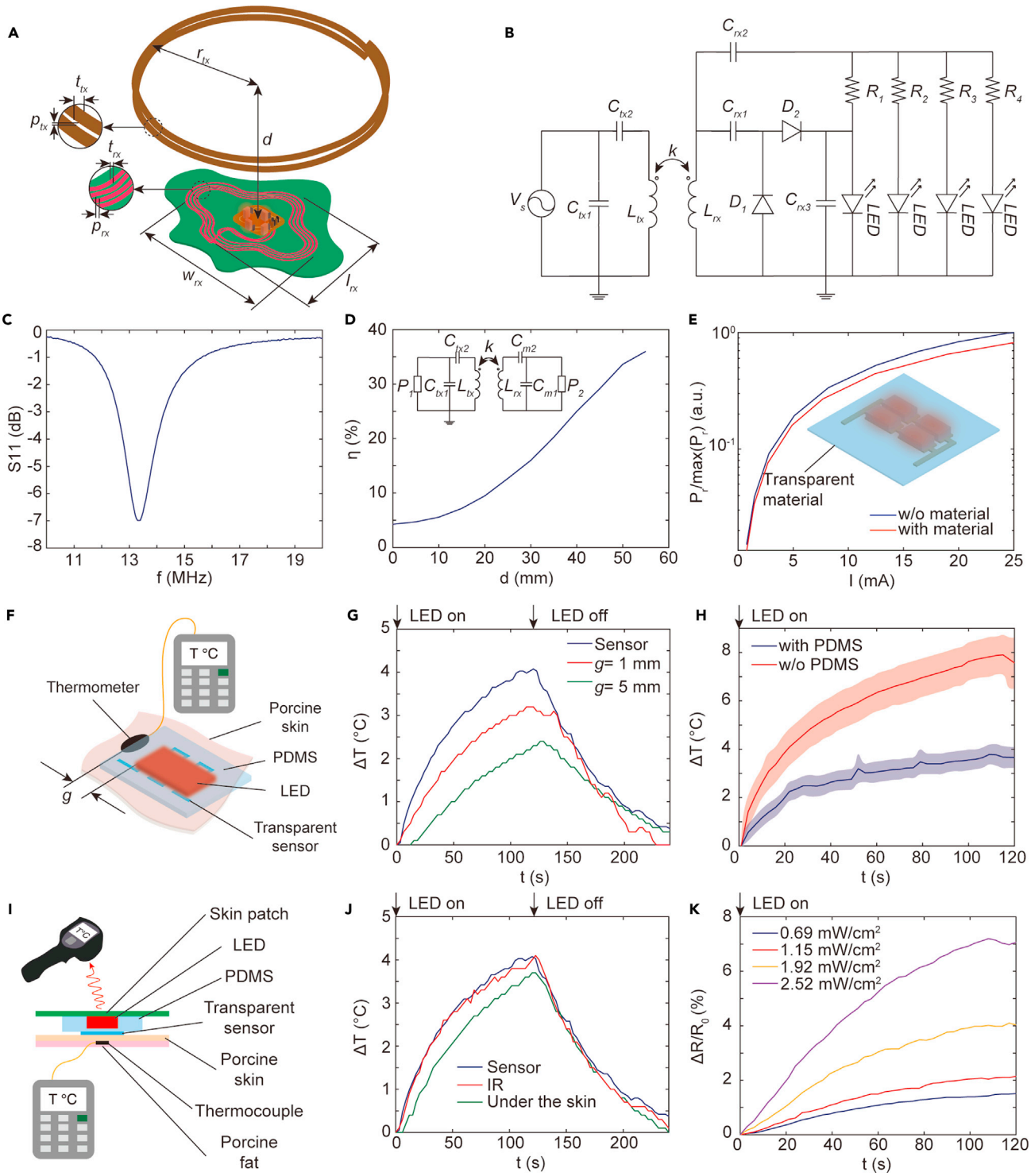

Figure 3. Design and performance of the wireless system

(A) System design parameters.

(B) Circuit diagram of the wireless transmitter (left) and optoelectronic patch (right).

(C) Reflection coefficient S_{11} of the optimized circuit measure from the load. The operating frequency is 13.56 MHz.

(D) Power transfer efficiency η as a function of the distance d between transmitter and device for C_{m1}=737 pF and C_{m2}=80 pF.

(E) Measured optical radiant power as a function of current I in the LED array with and without the transparent sensor.

(F) Illustration of the experimental setup using an adjacent thermocouple.

Figure 3. *Continued*

(G) Thermal monitoring comparison with a distant thermocouple. *g* is the distance between the thermocouple and LED array using setup in (F).

(H) Temperature change measured by the transparent sensor with and without thermal insulation (PDMS) using setup in (F). Graphs show mean and SD (n = 3 technical trials).

(I) Illustration of the experimental setup using infrared camera and subdermal thermocouple.

(J) Thermal monitoring comparison with an infrared (IR) sensor and a subdermal thermocouple using the setup in (I).

(K) Relative change in resistance of the transparent sensor when illuminating porcine skin at different power densities.

receive sufficient wireless power for light delivery while providing stable fixation on the back or wrist. The size and shape of the skin patch can be further customized for adhesion onto different body regions and wireless operating range.

Using a vector network analyzer configured with a 50-Ω matching circuit, we measured the wireless power transfer efficiency to characterize the range of the system. Figure 3D shows that the power transfer system achieves a maximum power transfer efficiency of 36% at a distance of 55 mm, which is sufficient for remote operation of the patch using a smartphone or a transmitter integrated into a bed. When the transmitter is brought closer to the patch, the efficiency decreases due to frequency splitting effects such that the efficiency drops to 4.6% when the distance is 0. Beyond 55 mm, the power transfer efficiency decreases monotonically because of weak coupling between the coils.

Owing to its high transparency, the presence of the sensor has a minimal impact on the radiant power transmitted through the LED array (Figure 3E). This property allows the sensor to accurately measure light-induced thermal effects on the skin, which is challenging to perform with sensors not co-located with the illumination region. We tested this capability by comparing temperature measurement using the transparent sensor and a thermocouple placed at different distances from the LED array when illuminating porcine skin (Figure 3F). For thermal insulation and encapsulation, the LED array is embedded within PDMS (Sylgard 184, Dow Corning USA) (Figure 3H), which minimizes heat transfer to the sensor due to resistive heating of the LED array (Zhang et al., 2018). Applying 36 dBm to the transmitter coil at a distance of 3 cm from the patch, thermal measurements from the transparent sensor detect tissue heating with a response time about 10 s earlier than the thermocouple. The measurements from the thermocouple are delayed and show a lower maximum temperature due to the distance from the light source (Figure 3G). This result highlights the importance of co-locating the sensor with the LED array to accurately assess the thermal effects of light delivery on tissue temperature. We also assessed the accuracy of the transparent sensor by comparing thermal measurements on porcine skin with an infrared thermal camera (E4, Teledyne FLIR LLC) and a subdermal thermocouple (Figure 3I). Although the infrared camera can provide a similar accuracy and response time to the transparent sensor, the resulting data have a higher noise due to the lack of contact with the target region. In contrast, the transparent sensor provides high-fidelity thermal monitoring and a form factor that can be integrated into a wearable device (Figure 3J). Measurements from the transparent sensor also show similar response times compared with the thermocouple, although the maximum temperature recorded by the thermocouple is slightly (~0.2°C) lower due to the subdermal location (Figure 3J). Measurements at varying levels of optical power further demonstrate the ability of the sensor to monitor different rates of light-induced heating on porcine skin (Figure 3K).

Demonstration of closed-loop light delivery and blood flow monitoring

We next demonstrate operation of the wireless optoelectronic patch on the human body for closed-loop light delivery and blood flow monitoring. The optoelectronic patch is mounted onto the back and the arm of the subject, as shown in Figures 4A and 4C. A transmitter placed above the patch provides wireless power transfer to activate the LED array, which emits light through the transparent sensor to the tissue surface. Thermal imaging in Figures 4B and 4D can be used to localize heating at the location of the LED array at the center of the skin patch during wireless power transfer at 41 dBm of input power on the transmitter coil. However, these images do not allow the skin temperature to be accurately measured because of confounding resistive heating effects and visual obstruction of the skin surface.

Figure 4E shows a flow diagram of the closed-loop control algorithm. The algorithm uses binary threshold control in which the LED is deactivated when the temperature exceeds a preset threshold, which can be determined depending on therapeutic and safety considerations (IEEE 2006). This simple technique is sufficient to maintain the time-averaged temperature at the set point, ensuring the long-term safety of the protocol. The system is also compatible with more advanced control algorithms based on fine-tuning of

Table 2. Parameters for coil design and equivalent circuit

Parameters	Length (mm)	Parameters	Description
r_{tx}	50	V_s	AC source (13.56 MHz)
N	2	L_{tx}	1.158 μH
t_{tx}	1	C_{tx1}	1.8 nF
p_{tx}	$\simeq$0	C_{tx2}	130 pF
w_{rx}	79.9	L_{rx}	1.78 μH
l_{rx}	56.7	C_{rx1}	680 pF
t_{rx}	0.16	C_{rx2}	82 pF
p_{rx}	3	C_{rx3}	680 pF
D	0–55	R_n	51 Ω
–	–	D_n	Schottky diode

the optical output power. For ease of experimentation, the set point temperature of the control loop is set to 36.2°C, which is well below the threshold for tissue damage (42°C). Figure 4F shows the temperature as the LED array is operated continuously without active control and with closed-loop control using the transparent sensor for the thermal measurement. Without control, the temperature of the LED array increases above 37°C, which exceeds the target of 36.2°C, whereas the closed loop maintains the time-average temperature near the target temperature. These results demonstrate that the transparent sensor can be used to regulate temperature in real time without requiring careful setup (such with the infrared camera) or compensation methods (optically opaque sensors). This capability has important implications for therapies involving high optical intensities, which pose risk of thermal damage to tissues, as well as diagnostic applications in which the sensor's accuracy can be improved by thermal calibration.

Continuous monitoring of hemodynamic activity is clinically relevant for the real-time detection of peripheral artery disorders (Webb et al. 2015b). Several wearable devices for blood flow monitoring have been developed based on electrical (Etemadi et al., 2015; Rosa et al., 2019; Cluff et al., 2017), mechanical (Etemadi et al., 2015; Wiens et al., 2014), acoustic (Rosa et al., 2019; Kenny 2021; Kenny et al., 2020), and optical (Abtahi et al. 2016; Saikia and Mankodiya 2018) approaches. In particular, photothermal method-based measurement of temperature gradients due to light-induced heating holds promise for integration into a lightweight wearable device, but currently relies on optically opaque thermal sensors that hinder accurate measurement. We applied the wireless optoelectronic patch in combination with four additional thermal sensors for measuring blood flow-related temperature gradients directly under the light source. Figure 4G shows the measurement setup in which the LED array is placed on the skin of a subject with visible left forearm veins directly above the radial artery. Two additional thermal sensors are placed proximally and distally at 10-mm intervals. The LED array optically elevates the temperature of the target artery, while the distributed thermal sensors measure the resulting thermal profile. Blood flow can then be quantified from the asymmetry in the spatiotemporal temperature distribution arising from anisotropic convective heat transfer. Figure 4H shows the measured temperature profiles resulting from a 1.8°C increase in skin temperature at the LED array. The temperature profiles exhibit clear asymmetry in both the time and amplitude of the peak, which can be used to estimate the blood flow (Webb et al. 2015a). Figure S1 presents additional results using a different arrangement of sensors. Proximal and distal thermal sensors placed around the LED show the same asymmetric temperature profile, whereas thermal sensors at equal distance away from the vein show symmetric thermal profiles because the blood flow is equal at the two points.

DISCUSSION

We have demonstrated a wireless optoelectronic patch that can be interfaced with the skin for light delivery and thermal monitoring. The patch integrates a transparent AgNW thermal sensor, fabricated using a laser-induced ablation process, which exhibits >92% optical transmission over the visible spectrum. The high transparency of the sensor allows direct measurement of the temperature of the skin without obstructing light delivery, enabling modes of operation that cannot be achieved using conventional sensors. Experimental studies demonstrate the use of the patch for closed-loop, thermally regulated light delivery as well as measurement of light-induced heating profiles to monitor blood flow dynamics. These capabilities can expand the function of wearable technologies for light-based sensing of hemodynamics, skin properties,

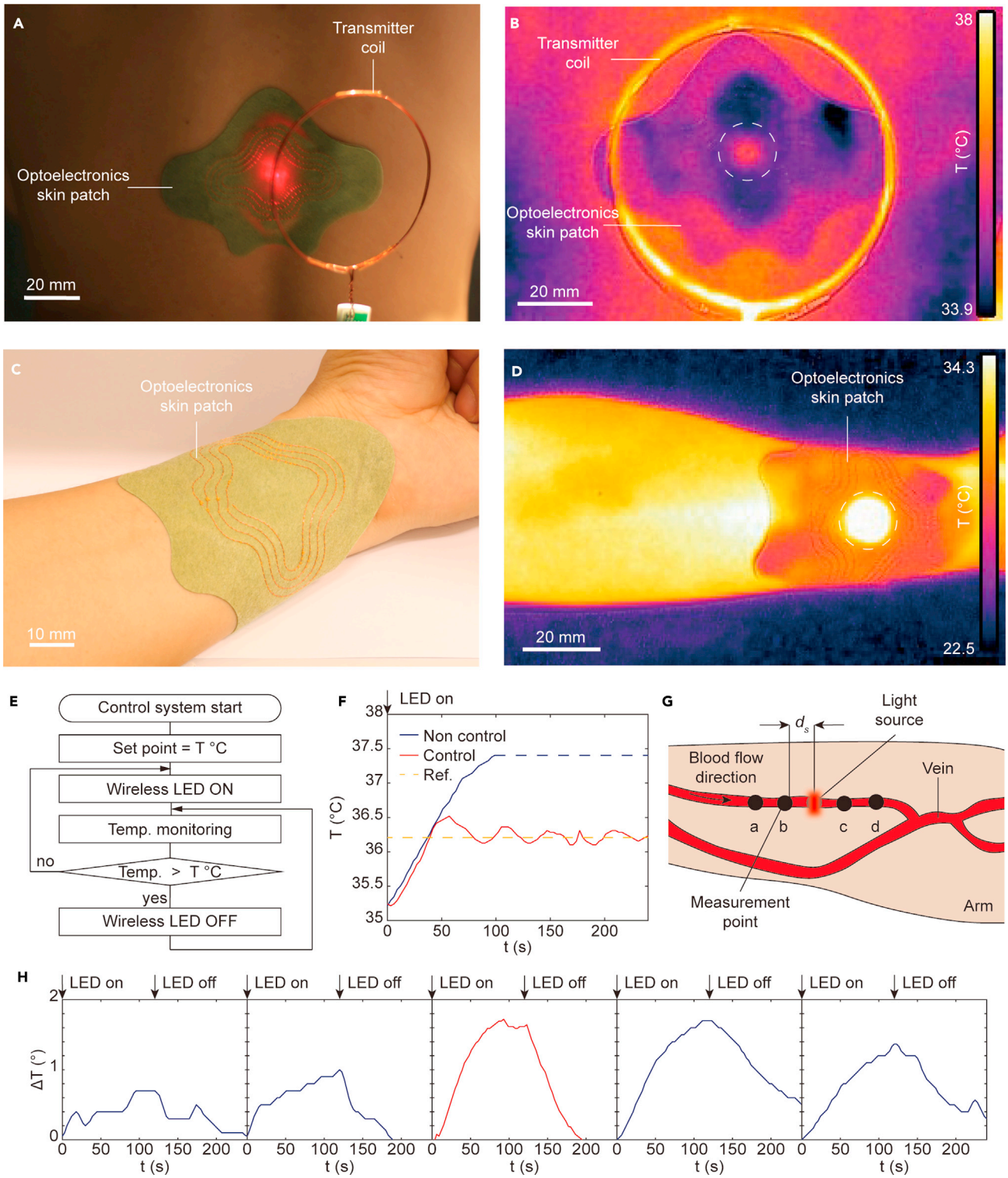

Figure 4. Closed-loop photothermal control and blood flow monitoring with a wireless patch

(A) Image of the optoelectronic patch attached to the lower back. The patch is wirelessly powered by a transmitter at a distance of 4 cm.

(B) Infrared thermal image of the activated patch during wireless powering. Dotted white circle indicates the position of the LED array.

(C) Image of the patch attached to the arm.

(D) Infrared thermal image of the activated patch on the wrist.

Figure 4. *Continued*
(E) Schematic of the closed-loop control algorithm.
(F) Skin temperature with and without closed-loop control using the setup in (A). The yellow dotted line indicates the target temperature of 36.2°C
(G) Schematic of the sensor placement along the radial artery using the setup in (C). The sensors are placed on the skin directly over the artery with spacing d_s=10 mm.
(H) Temperature as a function of time from each sensor when the LED array is activated for 120 s.

and other physiological properties, as well as for treatments such as photodynamic therapy and photobiomodulation.

The device can be further optimized for specific applications in optoelectronic sensing and therapy. For instance, the range and reliability of wireless power transfer can be improved for specific configurations, such as integration into a bed, and incorporating power management circuits. A rechargeable small battery can also be integrated into the patch to allow use outside of the range of the wireless system. The LED array can be customized considering the desired wavelength and optical irradiation power and the tolerated thermal effect. For example, photodynamic therapy may require multiwavelength emission to optimally activate photosensitizers (Bansal et al., 2018), whereas near-infrared wavelengths may be preferable to deliver energy into deeper tissue regions for sensing applications (Lee et al. 2020a). Clinical validation studies will be required to establish the performance of the wearable optoelectronic device compared with the gold standard, such as Doppler ultrasound for blood flow monitoring (Kenny 2021; Kenny et al., 2020). Additional modalities, such as impedance cardiography (Cluff et al., 2017) and reflectometry (Saikia and Mankodiya 2018), can also be incorporated to improve sensing accuracy.

The transparent sensor can also be optimized to achieve different ranges of resistance and geometric patterns by tuning the density of the AgNW network. Such optimization could be used to maximize the sensitivity of the digital readout by operating within the ideal range of the amplifier and analog-to-digital converter. Beyond the visible spectrum, applications in the near-infrared and UV regions are also of interest for the treatment of psoriasis (Stern 2007), mood disorder (Parry and Maurer 2003), wound infections (Eells et al., 2004), and neurodegeneration (Johnstone et al., 2016), although further characterization and optimization of the sensor's transparency at these wavelengths is required. Future work may also explore implantable versions of the device for clinical applications in metronomic therapy and monitoring of deep tissue sites.

Limitations of the study

Although the frequency of wireless operation is compatible with smartphone-based NFC, NFC chipsets need to be integrated to allow bidirectional communication. Furthermore, rigorous clinical studies are required to determine the impact of the technology for different use cases in light-based diagnosis and therapy.

STAR★METHODS

Detailed methods are provided in the online version of this paper and include the following:

- KEY RESOURCES TABLE
- RESOURCE AVAILABILITY
  - Lead contact
  - Materials availability
  - Data and code availability
- METHOD DETAILS
  - Materials and reagents
  - Fabrication and characterization of transparent temperature sensors
  - Fabrication of the skin patch
  - Wireless power transfer system
  - Light delivery design and characterization
  - On-body demonstration
- QUANTIFICATION AND STATISTICAL ANALYSIS
  - Statistical analysis

SUPPLEMENTAL INFORMATION

Supplemental information can be found online at https://doi.org/10.1016/j.isci.2021.103284.

ACKNOWLEDGMENTS

This work was supported by grants from the National Research Foundation Singapore (Grant No. NRF-NRFF 2017-07), Ministry of Education Singapore (Grants No. MOE2016-T3-1-004), Institute for Health Innovation and Technology, and N.1 Institute for Health.

AUTHOR CONTRIBUTIONS

Conceptualization and project design, J.S.H.; sensor design, fabrication, and characterization, Y.J. and J.S.H.; coil and circuit design, fabrication, and characterization, S.A., H.-J.K., and J.S.H.; skin patch coil fabrication, R.L.; experimental design, performance, and analysis, H.-J.K.; supervision, J.S.H.; writing, H.-J.K., Y.J., and J.S.H.

DECLARATION OF INTERESTS

The authors declare no competing interests.

Received: April 26, 2021
Revised: August 31, 2021
Accepted: October 13, 2021
Published: November 19, 2021

REFERENCES

Abtahi, M., Cay, G., Saikia, M.J., and Mankodiya, K. (2016). Designing and testing a wearable, wireless fnirs patch. In 2016 38th Annual International Conference of the IEEE Engineering in Medicine and Biology Society (EMBC) (IEEE), pp. 6298–6301.

Bansal, A., Yang, F., Xi, T., Zhang, Y., and Ho, J.S. (2018). In vivo wireless photonic photodynamic therapy. Proc. Natl. Acad. Sci. U S A *115*, 1469–1474.

Bashkatov, A., Genina, E., Kochubey, V., and Tuchin, V. (2005). Optical properties of human skin, subcutaneous and mucous tissues in the wavelength range from 400 to 2000 nm. J. Phys. D Appl. Phys. *38*, 2543.

Bäumler, W. (2001). Light sources for photodynamic therapy and fluorescence diagnosis in dermatology. In Comprehensive Series in Photosciences, *2*, P. Calzavara-Pinton, R.-M. Szeimies, and B. Ortel, eds. (Elsevier), pp. 83–98.

Beigzadeh, A.M., Rashidian Vaziri, M.R., Ziaie, F., and Sharif, S. (2020). A new optical method for online monitoring of the light dose and dose profile in photodynamic therapy. Lasers Surg. Med. *52*, 659–670.

Bi, Y.G., Liu, Y.F., Zhang, X.L., Yin, D., Wang, W.Q., Feng, J., and Sun, H.B. (2019). Ultrathin metal films as the transparent electrode in ito-free organic optoelectronic devices. Adv. Opt. Mater. *7*, 1800778.

Blouin, A.G., Blouin, J.H., Iversen, H., Carter, J., Goldstein, C., Goldfield, G., and Perez, E. (1996). Light therapy in bulimia nervosa: a double-blind, placebo-controlled study. Psychiatry Res. *60*, 1–9.

Choi, J.H., Shin, M.G., Jung, Y., Kim, D.H., and Ko, J.S. (2020). Fabrication and performance evaluation of highly sensitive flexible strain sensors with aligned silver nanowires. Micromachines *11*, 156.

Chung, H., Dai, T., Sharma, S.K., Huang, Y.Y., Carroll, J.D., and Hamblin, M.R. (2012). The nuts and bolts of low-level laser (light) therapy. Ann. Biomed. Eng. *40*, 516–533.

Cluff, K., Becker, R., Jayakumar, B., Han, K., Condon, E., Dudley, K., Szatkowski, G., Pipinos, I.I., Amick, R.Z., and Patterson, J. (2017). Passive wearable skin patch sensor measures limb hemodynamics based on electromagnetic resonance. IEEE Trans. Biomed. Eng. *65*, 847–856.

Cortezon-Tamarit, F., Ge, H., Mirabello, V., Theobald, M.B., Calatayud, D.G., and Pascu, S. (2017). Carbon nanotubes and related nanohybrids incorporating inorganic transition metal compounds and radioactive species as synthetic scaffolds for nanomedicine design. In Inorganic and Organometallic Transition Metal Complexes with Biological Molecules and Living Cells, K. Lo, ed. (Elsevier), pp. 245–327.

Cui, Z., Poblete, F.R., and Zhu, Y. (2019). Tailoring the temperature coefficient of resistance of silver nanowire nanocomposites and their application as stretchable temperature sensors. ACS Appl. Mater. Interfaces *11*, 17836–17842.

Devor, A., Sakadžić, S., Srinivasan, V.J., Yaseen, M.A., Nizar, K., Saisan, P.A., Tian, P., Dale, A.M., Vinogradov, S.A., Franceschini, M.A., et al. (2012). Frontiers in optical imaging of cerebral blood flow and metabolism. J. Cereb. Blood Flow Metab. *32*, 1259–1276.

Dolmans, D.E., Fukumura, D., and Jain, R.K. (2003). Photodynamic therapy for cancer. Nat. Rev. Cancer *3*, 380–387.

Eells, J.T., Wong-Riley, M.T., VerHoeve, J., Henry, M., Buchman, E.V., Kane, M.P., Gould, L.J., Das, R., Jett, M., Hodgson, B.D., et al. (2004). Mitochondrial signal transduction in accelerated wound and retinal healing by near-infrared light therapy. Mitochondrion *4*, 559–567.

Eskiizmir, G., Ermertcan, A.T., and Yapici, K. (2017). Nanomaterials: promising structures for the management of oral cancer. In Nanostructures for Oral Medicine, E. Andronescu and G. Alexandru, eds. (Elsevier), pp. 511–544.

Etemadi, M., Inan, O.T., Heller, J.A., Hersek, S., Klein, L., and Roy, S. (2015). A wearable patch to enable long-term monitoring of environmental, activity and hemodynamics variables. IEEE Trans. Biomed. circuits Syst. *10*, 280–288.

Fritsch, C., Goerz, G., and Ruzicka, T. (1998). Photodynamic therapy in dermatology. Arch. Dermatol. *134*, 207–214.

Gao, L., Zhang, Y., Malyarchuk, V., Jia, L., Jang, K.I., Webb, R.C., Fu, H., Shi, Y., Zhou, G., Shi, L., et al. (2014). Epidermal photonic devices for quantitative imaging of temperature and thermal transport characteristics of the skin. Nat. Commun. *5*, 1–10.

Garbarino, M., Lai, M., Bender, D., Picard, R.W., and Tognetti, S. (2014). Empatica e3–a wearable wireless multi-sensor device for real-time computerized biofeedback and data acquisition. In 2014 4th International Conference on Wireless Mobile Communication and Healthcare-Transforming Healthcare through Innovations in Mobile and Wireless Technologies (MOBIHEALTH) (IEEE), pp. 39–42.

Hamblin, M.R., Huang, Y.Y., and Heiskanen, V. (2019). Non-mammalian hosts and photobiomodulation: do all life-forms respond to light? Photochem. Photobiol. *95*, 126–139.

IEEE (2006). IEEE standard for safety with respect to human exposure to radiofrequency electromagnetic fields, 3 kHz to 300 GHz. IEEE Stand. *C95*, 1–2005.

Jeong, H., Wang, L., Ha, T., Mitbander, R., Yang, X., Dai, Z., Qiao, S., Shen, L., Sun, N., and Lu, N. (2019). Modular and reconfigurable wireless e-tattoos for personalized sensing. Adv. Mater. Tech. *4*, 1900117.

Jin, Y., Li, L., Cheng, Y., Kong, L., Pei, Q., and Xiao, F. (2015). Cohesively enhanced conductivity and adhesion of flexible silver nanowire networks by biocompatible polymer sol–gel transition. Adv. Funct. Mater. *25*, 1581–1587.

Jin, Y., Sun, Y., Wang, K., Chen, Y., Liang, Z., Xu, Y., and Xiao, F. (2018). Long-term stable silver nanowire transparent composite as bottom electrode for perovskite solar cells. Nano Res. *11*, 1998–2011.

Jinno, H., Yokota, T., Koizumi, M., Yukita, W., Saito, M., Osaka, I., Fukuda, K., and Someya, T. (2021). Self-powered ultraflexible photonic skin for continuous bio-signal detection via air-operation-stable polymer light-emitting diodes. Nat. Commun. *12*, 1–9.

Johnstone, D.M., Moro, C., Stone, J., Benabid, A.L., and Mitrofanis, J. (2016). Turning on lights to stop neurodegeneration: the potential of near infrared light therapy in alzheimer's and Parkinson's disease. Front. Neurosci. *9*, 500.

Juarranz, Á., Jaén, P., Sanz-Rodríguez, F., Cuevas, J., and González, S. (2008). Photodynamic therapy of cancer. basic principles and applications. Clin. Transl. Oncol. *10*, 148–154.

Kang, M.H., Lee, G.J., Lee, J.H., Kim, M.S., Yan, Z., Jeong, J.W., Jang, K.I., and Song, Y.M. (2021). Outdoor-useable, wireless/battery-free patch-type tissue oximeter with radiative cooling. Adv. Sci. *8*, 2004885.

Kenny, J.É.S. (2021). Functional hemodynamic monitoring with a wireless ultrasound patch. J. Cardiothorac. Vasc. Anesth. *35*, 1509–1515.

Kim, B.S., Kim, M.K., Jo, D.S., Chae, H., and Cho, S.M. (2017a). Optimal structure of color-conversion layer for white organic light-emitting diode on silver-nanowire anode. ECS J. Solid State Sci. Technol. *7*, R3176.

Kenny, J.É.S., Barjaktarevic, I., Mackenzie, D.C., Eibl, A.M., Parrotta, M., Long, B.F., and Eibl, J.K. (2020). Diagnostic characteristics of 11 formulae for calculating corrected flow time as measured by a wearable Doppler patch. Intensive Care Med. Exp. *8*, 1–11.

Khan, Y., Han, D., Pierre, A., Ting, J., Wang, X., Lochner, C.M., Bovo, G., Yaacobi-Gross, N., Newsome, C., Wilson, R., et al. (2018). A flexible organic reflectance oximeter array. Proc. Natl. Acad. Sci.U S A *115*, E11015–E11024.

Kim, J., Gutruf, P., Chiarelli, A.M., Heo, S.Y., Cho, K., Xie, Z., Banks, A., Han, S., Jang, K.I., Lee, J.W., et al. (2017b). Miniaturized battery-free wireless systems for wearable pulse oximetry. Adv. Funct. Mater. *27*, 1604373.

Lee, G.H., Moon, H., Kim, H., Lee, G.H., Kwon, W., Yoo, S., Myung, D., Yun, S.H., Bao, Z., and Hahn, S.K. (2020a). Multifunctional materials for implantable and wearable photonic healthcare devices. Nat. Rev. Mater. *5*, 149–165.

Kim, J., Salvatore, G.A., Araki, H., Chiarelli, A.M., Xie, Z., Banks, A., Sheng, X., Liu, Y., Lee, J.W., Jang, K.I., et al. (2016). Battery-free, stretchable optoelectronic systems for wireless optical characterization of the skin. Sci. Adv. *2*, e1600418.

Langley, D., Giusti, G., Mayousse, C., Celle, C., Bellet, D., and Simonato, J.P. (2013). Flexible transparent conductive materials based on silver nanowire networks: a review. Nanotechnology *24*, 452001.

Lee, S., Kim, S.W., Ghidelli, M., An, H.S., Jang, J., Bassi, A.L., Lee, S.Y., and Park, J.U. (2020b). Integration of transparent supercapacitors and electrodes using nanostructured metallic glass films for wirelessly rechargeable, skin heat patches. Nano Lett. *20*, 4872–4881.

Parry, B.L., and Maurer, E.L. (2003). Light treatment of mood disorders. Dialogues Clin. Neurosci. *5*, 353.

Ren, W., Yan, Y., Zeng, L., Shi, Z., Gong, A., Schaaf, P., Wang, D., Zhao, J., Zou, B., Yu, H., et al. (2015). A near infrared light triggered hydrogenated black tio2 for cancer photothermal therapy. Adv. Healthc. Mater. *4*, 1526–1536.

Rosa, B.M.G., Anastasova-Ivanova, S., and Yang, G.Z. (2019). NFC-powered flexible chest patch for fast assessment of cardiac, hemodynamic, and endocrine parameters. IEEE Trans. Biomed. Circuits Syst. *13*, 1603–1614.

Safaie, J., Grebe, R., Moghaddam, H.A., and Wallois, F. (2013). Toward a fully integrated wireless wearable eeg-nirs bimodal acquisition system. J. Neural Eng. *10*, 056001.

Saikia, M.J., and Mankodiya, K. (2018). A wireless fnirs patch with short-channel regression to improve detection of hemodynamic response of brain. In 2018 International Conference on Electrical, Electronics, Communication, Computer, and Optimization Techniques (ICEECCOT) (IEEE), pp. 90–96.

Shao, J., Xie, H., Huang, H., Li, Z., Sun, Z., Xu, Y., Xiao, Q., Yu, X.F., Zhao, Y., Zhang, H., et al. (2016). Biodegradable black phosphorus-based nanospheres for in vivo photothermal cancer therapy. Nat. Commun. *7*, 1–13.

Shin, Y.B., Ju, Y.H., Seo, I.S., Lee, C.R., Kim, Y.n., jun Kong, K., and Kim, J.W. (2020). Modified inverted layer processing of ultrathin touch sensor impregnating ag nanowires with both enlarged surface coverage of conductive pathways and ultralow roughness. Electron. Mater. Lett. *16*, 247–254.

Stern, R.S. (2007). Psoralen and ultraviolet a light therapy for psoriasis. N. Engl. J. Med. *357*, 682–690.

Tang, H., Feng, H., Wang, H., Wan, X., Liang, J., and Chen, Y. (2019). Highly conducting mxene–silver nanowire transparent electrodes for flexible organic solar cells. ACS Appl. Mater. Interfaces *11*, 25330–25337.

Terman, M., and Terman, J.S. (2005). Light therapy. In Principles and Practice of Sleep Medicine, 4th ed., M. Kryger, T. Roth, and W. Dement, eds. (Elsevier), pp. 1424–1442.

Thomas, J.P., Rahman, M.A., Srivastava, S., Kang, J.S., McGillivray, D., Abd-Ellah, M., Heinig, N.F., and Leung, K.T. (2018). Highly conducting hybrid silver-nanowire-embedded poly (3, 4-ethylenedioxythiophene): poly (styrenesulfonate) for high-efficiency planar silicon/organic heterojunction solar cells. ACS Nano *12*, 9495–9503.

Wang, Y.F., Sekine, T., Takeda, Y., Yokosawa, K., Matsui, H., Kumaki, D., Shiba, T., Nishikawa, T., and Tokito, S. (2020). Fully printed pedot: Pss-based temperature sensor with high humidity stability for wireless healthcare monitoring. Sci. Rep. *10*, 1–8.

Watthanawisuth, N., Lomas, T., Wisitsoraat, A., and Tuantranont, A. (2010). Wireless wearable pulse oximeter for health monitoring using zigbee wireless sensor network. In ECTI-CON2010: The 2010 ECTI International Confernce on Electrical Engineering/Electronics, Computer, Telecommunications and Information Technology (IEEE), pp. 575–579.

Webb, R.C., Ma, Y., Krishnan, S., Li, Y., Yoon, S., Guo, X., Feng, X., Shi, Y., Seidel, M., Cho, N.H., et al. (2015a). Epidermal devices for noninvasive, precise, and continuous mapping of macrovascular and microvascular blood flow. Sci. Adv. *1*, e1500701.

Webb, R.C., Pielak, R.M., Bastien, P., Ayers, J., Niittynen, J., Kurniawan, J., Manco, M., Lin, A., Cho, N.H., Malyrchuk, V., et al. (2015b). Thermal transport characteristics of human skin measured in vivo using ultrathin conformal arrays of thermal sensors and actuators. PLoS One *10*, e0118131.

Wiens, A.D., Etemadi, M., Roy, S., Klein, L., and Inan, O.T. (2014). Toward continuous, noninvasive assessment of ventricular function and hemodynamics: wearable ballistocardiography. IEEE J. Biomed. Health Inform. *19*, 1435–1442.

Wilson, B.C., and Patterson, M.S. (2008). The physics, biophysics and technology of photodynamic therapy. Phys. Med. Biol. *53*, R61.

Wu, X., Zhou, Z., Wang, Y., and Li, J. (2020). Syntheses of silver nanowires ink and printable flexible transparent conductive film: a review. Coatings *10*, 865.

Wyser, D.G., Lambercy, O., Scholkmann, F., Wolf, M., and Gassert, R. (2017). Wearable and modular functional near-infrared spectroscopy instrument with multidistance measurements at four wavelengths. Neurophotonics *4*, 041413.

Yang, H., Bai, S., Chen, T., Zhang, Y., Wang, H., and Guo, X. (2019). Facile fabrication of large-scale silver nanowire-pedot: Pss composite flexible transparent electrodes for flexible touch panels. Mater. Res. Express *6*, 086315.

Yang, Y., Chen, S., Li, W., Li, P., Ma, J., Li, B., Zhao, X., Ju, Z., Chang, H., Xiao, L., et al. (2020). Reduced graphene oxide conformally wrapped silver nanowire networks for flexible transparent heating and electromagnetic interference shielding. ACS Nano *14*, 8754–8765.

Yu, J.W., Lim, S.H., Kim, B., Kim, E., Kim, K., Park, S.K., Byun, Y.S., Sakong, J., and Choi, J.W. (2020). Prefrontal functional connectivity analysis of cognitive decline for early diagnosis of mild cognitive impairment: a functional near-infrared spectroscopy study. Biomed. Opt. Express *11*, 1725–1741.

Zhang, Y.X., Fang, J., Li, W., Shen, Y., Chen, J.D., Li, Y., Gu, H., Pelivani, S., Zhang, M., Li, Y., et al. (2019a). Synergetic transparent electrode architecture for efficient non-fullerene flexible organic solar cells with¿ 12% efficiency. ACS Nano *13*, 4686–4694.

Yun, S.O., Lee, J.H., Lee, J., and Kim, C.Y. (2019). A flexible wireless sensor patch for real-time monitoring of heart rate and body temperature. IEICE Trans. Inf. Syst. *102*, 1115–1118.

Zein, R., Selting, W., and Hamblin, M.R. (2018). Review of light parameters and photobiomodulation efficacy: dive into complexity. J. Biomed. Opt. *23*, 120901.

Zhang, Z., Alwen, A., Lyu, H., Liu, X., Li, Z., Xie, Z., Xie, Y., Guan, F., Babakhani, A., and Pei, Q. (2019b). Stretchable transparent wireless charging coil fabricated by negative transfer printing. ACS Appl. Mater. Interfaces *11*, 40677–40684.

Zhang, C., Qu, L., Wang, Y., Xu, T., and Zhang, C. (2018). Thermal insulation and stability of polysiloxane foams containing hydroxyl-terminated polydimethylsiloxanes. RSC Adv. *8*, 9901–9909.

Zhang, H., Zhao, H., Zhao, X., Xu, C., Franklin, D., Vázquez-Guardado, A., Bai, W., Zhao, J., Li, K., Monti, G., et al. (2021). Biocompatible light guide-assisted wearable devices for enhanced uv light delivery in deep skin. Adv. Funct. Mater. *31*, 2100576.

STAR★METHODS

KEY RESOURCES TABLE

REAGENT or RESOURCE	SOURCE	IDENTIFIER
Chemicals, peptides, and recombinant proteins		
Silver paint	Ted Pella, INC.	Pelco silver paint (16062)
Sylgard 184	DOW Corning USA	Material Number 1024001
Epoxy adhesive	Araldite	Ara5m
Software and algorithms		
Embroidery design software	Brother	PE-DESIGN 10
3D Electromagnetic software	Dassault Systemes	CST Studio Suite
Other		
Laser cutter	Universal Laser Systems	VLS 2.30
Embroidery machine	Brother	NV 180
UV/Visible spectrum	Shimazu	UV-1800
Optical power meter	Newport	2935-C
Photodetector	Newport	918D-UV-OD3R
Scanning electron microscope	Thermo Scientific	FEI Verios 460
DC power supplier	Tenma	72-2690
Signal generator	Rohde & Schwarz	SMA 100A
Power amplifier	Mini circuit	LZY-22+
Vector network analyzer	Keysight	N9915A FieldFox Handheld Microwave Analyzer
Multimeter	Fluke	289
Thermocouple	Omega	HH506RA
Infrared camera	FLIR	E4
Polyethy- lene terephthalate (PET) film	Zhejiang Kechuang Advanced Materials Co., LTD.	100 μm
Copper thread	Belden Inc.	BEL 1985-ND
Light emitting diode (LED) 660 nm	Lumex	SML-LW0603RW-TR
Schottky diode	Infineon Technologies	BAT2402LSE6327XTSA1CT-ND

RESOURCE AVAILABILITY

Lead contact

Further information and requests for resources and reagents should be directed to and will be fulfilled by the lead contact, John S. Ho (johnho@nus.edu.sg).

Materials availability

This study did not generate new unique reagents.

Data and code availability

- All data reported in this paper will be shared by the lead contact upon request.
- This paper does not report original code.
- Any additional information required to reanalyze the data reported in this paper is available from the lead contact upon request.

METHOD DETAILS

Materials and reagents

Silver nanowire (30 nm diameter, 10-15 μm length) dispersion was purchased from Zhejiang Kechuang Advanced Materials Co., Ltd. 100 μm thick polyethylene terephthalate (PET) film was used as the substrate

for the transparent sensor. Electrical connections to the sensor used Pelco silver paint (16062, Ted Pella, Inc).

Fabrication and characterization of transparent temperature sensors

Conductive film preparation: The AgNW dispersion was diluted from 1 wt% to 0.1 wt% with isopropyl alcohol. The dispersion was sonicated for 5 sec to uniformly disperse the nanowires in solvent, followed by 5 min of manual shaking. PET was cleaned with deionized water, alcohol, and acetone, and then oven-dried. To increase hydrophilicity, the surface was treated with plasma (50 W, 30 s). The AgNW dispersion was rod-coated on PET film to form a conductive nanowire network, and a thin layer of rGO further applied to weld the nanowire junctions. Conductivity was adjusted by varying the coating time to tune the density of the nanowire network.

Sensor patterning: AgNW patterns were formed using a laser cutter (VLS 2.30 Universal Laser Systems). The laser was scanned in raster mode at 4% energy and 3% moving speed. The total footprint area of the sensor was 1.5×2 mm. The sensor was connected to the device by encapsulating metal wires on the pads using Pelco silver paint cured at 100°C on a hotplate for 5 min.

Characterization: Surface morphology was obtained using a scanning electron microscope (FEI Verios 460). Transmittance in the UV/Visible spectrum was obtained using a UV-Vis Spectrophotometer (Shimadzu UV-1800). Electrical resistance data was acquired using a multimeter (Fluke, 289).

Fabrication of the skin patch

The inductor pattern was designed using electromagnetic design software (CST Studio Suite, Dassault Systemes). The final pattern was transferred as a vector image (Figure S2A) to a digital embroidery tool (PE-DESIGN 10, Brother). The pattern was reproduced on a fabric skin patch (Ai Yi Shi) using an embroidery machine (NV180, Brother) fed with copper thread (BEL 1985-ND, Belden Inc). The LED array and wireless powering circuit was assembled on a custom flexible printed circuit board (Interhorizon Corporation Pte Ltd) by manual soldering. The circuit board was connected to the embroidered inductive pattern by soldering the copper wires to the ports indicated in Figures S2C and S2D. Epoxy adhesive (Ara5m, Araldite) was applied to the junction and the circuit board for protection. The fabrication process was easily reproducible (2 devices) because it is based on standard processes.

Wireless power transfer system

Wireless powering used a transmitter coil operating in the 13.56 MHz industrial, scientific, and medical band. The transmitter coil was driven using a signal generator (SMB100A, Rohde & Schwarz) connected to a power amplifier (LZY-22+, Mini Circuits). The wireless performance was evaluated by measuring the scattering parameters between the device and the transmitter coil using a vector network analyzer (N9915A FieldFox Handheld Microwave Analyzer, Keysight). The impedances of the coils were matched to the source and load using L-type matching circuits. The power transfer efficiency was measured via the scattering parameter S_{21}. Displacement measurements were performed by clamping the device to a translational stage while keeping the position of the transmitter coil constant.

Light delivery design and characterization

Light delivery used an array of four red surface-mounted LEDs (SML-LX0603SRW-TR, Lumex) driven in parallel by the wireless power system or, in characterization experiments, a DC power supply (72-2690, Tenma). A voltage doubler, comprising Schottky diodes (BAT2402LSE6327XTSA1CT-ND, Infineon Technologies) and chip capacitors, was used to rectify the signal at the output of the receiver coil. The LED array was encapsulated in PDMS and the transparent temperature sensor attached onto the PDMS surface. Characterization experiments used an optical power meter (2935-C, Newport) and photodetector (918D-UV-OD3R, Newport) for optical transmission measurements. On-skin experiments used porcine skin and either a thermocouple (HH506RA, Omega) or infrared camera (E4, FLIR Systems) for comparisons.

On-body demonstration

The wireless skin patch was attached to the back of the subject (healthy male volunteer, age between 30–40) and powered by the wireless transmitter. The transparent sensor data was acquired using a multimeter (289, Fluke). The skin patch is attached above the radial artery near the wrist for blood flow mapping.

The transparent sensor was located under the LED and connect to a multimeter (289, Fluke). The temperature at other measurement points was monitored using a thermocouple (HH506RA, Omega). Thermal images were acquired by an infrared camera (E4, FLIR Systems). All experiments complied with a protocol approved by the National University of Singapore Institutional Review Board. The subject was a volunteer, was informed of risks and benefits, and provided informed consent.

QUANTIFICATION AND STATISTICAL ANALYSIS

Statistical analysis

Optical and electrical characterization of the transparent thermal sensor (Figures 2E–2G) show representative results from one out of four fabricated sensors. No significant variability was observed between sensors. Wireless system measurements (Figures 3C–3E) show results obtained from one device assembled from commercially available circuit components. Thermal experiments using porcine skin show single trial (Figures 3G, 3J, and 3K) or mean and standard deviation from three technical trials (Figure 3H). On-body thermal measurements (Figure 4) were obtained from one subject as this was sufficient to demonstrate the optoelectronic functionality of the device.